RSC Advances

PAPER

View Article Online
View Journal | View Issue

Cite this: *RSC Adv.*, 2017, 7, 15903

# Direct *in situ* synthesis of a 3D interlinked amorphous carbon nanotube/graphene/$BaFe_{12}O_{19}$ composite and its electromagnetic wave absorbing properties

Tingkai Zhao,†[a] Xianglin Ji,†*[a] Wenbo Jin,[a] Chuan Wang,[a] Wenxiu Ma,[a] Junjie Gao,[a] Alei Dang,[a] Tiehu Li,[a] Songmin Shang[b] and Zhongfu Zhou[c]

Received 16th January 2017
Accepted 6th March 2017

DOI: 10.1039/c7ra00623c

rsc.li/rsc-advances

The 3D interlinked amorphous carbon nanotube (ACNT)/reduced graphene oxide (RGO)/$BaFe_{12}O_{19}$ (BF) composite was directly prepared by a self-propagation combustion process. The RGO was synthesized *in situ* through the massive heat release during the auto-combustion reaction. The interlinked ACNTs and graphene as well as BF formed the conductive networks for improving the dielectric and magnetic loss. The reflection loss peak of ACNT/RGO/BF composite was −19.03 dB at 11.04 GHz in the frequency range of 2–18 GHz. The frequency bandwidth of the reflection loss below −10 dB was 3.8 GHz. The 3D interlinked ACNT-RGO structure, which was composed of dense intertwined ACNT and graphene with quantities of dihedral angles, could consume incident waves *via* multiple reflections inside the 3D structures. The high conductivity of 3D interlinked ACNT/RGO networks would lead to energy dissipation in the form of heat through molecular friction and dielectric loss.

## 1. Introduction

Electromagnetic wave absorbing materials have been a hot-topic research in recent years due to their outstanding potential applications in many fields, such as electric devices, mobile screens, and military arms, *etc.*[1] Generally, the main target for traditional absorbing materials would be to have strong absorption, which is accompanied with a narrow absorption bandwidth, high density and other shortcomings.[2] However, some nanosized composites have the characteristics of adjustable electromagnetic properties and high coercive forces. So the nanocomposites that were used as electromagnetic wave absorbers could meet the requirements of "thin thickness, wide bandwidth, lightweight and strong adsorption". Therefore, the development of nanocomposites, especially based on carbon materials, in the field of electromagnetic wave absorption is very important.[3–5]

Graphene is a lightweight and good electrical conductivity new carbon material, which has excellent mechanical, optical, thermal and electrical properties.[6] In particular, the high dielectric constant and the susceptibility of the outer electrons to the polarized relaxation of graphene make it as a potential dielectric loss material, which could be widely used in the field of electromagnetic wave absorption.[7,8] In addition, graphene oxide (GO) is an ideal supporter because it contains a large number of polar functional groups, surface area and ion exchange capacity. At present, GO as electromagnetic wave absorbing material is usually compound with other absorber materials.[9–11]

Carbon nanotubes (CNTs) have extremely high mechanical strength and toughness, good electrical conductivity, excellent thermal conductivity and electromagnetic compatibility.[12–14] It dissipates the electromagnetic wave through static electricity and radar technology. These properties provide great potential application of CNTs in electromagnetic wave absorption field. Especially, the tube-wall structures of amorphous carbon nanotubes (ACNTs) have the characteristics of short-range order and long-range disorder. It has significantly dielectric loss due to the good conductivity. The impedance of ACNTs is close to the impedance of free space, which could match each other exceedingly well.[15]

Hexagonal M-type $BaFe_{12}O_{19}$ (BF) with a single-axis magnetocrystalline anisotropy and high coercivity could present strong magnetic loss. It is widely used as a permanent magnet and microwave absorption material because of its easy preparation, low cost and chemical stability.[16,17] Hexagonal M-type BF owns strong absorption in a wide frequency range, which is suitable for the production of matching layer. BF has good

---

[a] *State Key Laboratory of Solidification Processing, Shaanxi Engineering Laboratory for Graphene New Carbon Materials and Applications, School of Materials Science and Engineering, Northwestern Polytechnical University, Xi'an 710072, China. E-mail: ztk-xjtu@163.com; jixianglinnwpu@163.com*

[b] *Institute of Textiles and Clothing, The Hong Kong Polytechnic University, Kowloon, Hong Kong*

[c] *Department of Physics, Aberystwyth University, Aberystwyth SY23 3FL, UK*

† T. K. Zhao and X. L. Ji contribute equally to this work.

potential applications in the electromagnetic wave absorption field.[18] However, the applications of BF are limited due to the poor dielectric constant. Nowadays, the absorber nanocomposites consisting of both dielectric and magnetic fillers have attracted researchers much attention. ACNTs or/and graphene compounded with BF would possess both the good dielectric loss and magnetic loss characteristics. Three-dimensional (3D) conductive networks of the interlinked CNTs and RGO were formed inside barium ferrite. It makes them contact tightly for increasing the resonance circuit density and attenuating the electromagnetic radiation in the absorbers effectively.

In this paper, ACNT/RGO/BF composite was *in situ* synthesized. The electromagnetic wave absorption properties were studied. The barium ferrite with high permeability and coercivity can easily widen absorption bandwidth and further enhance reflection loss. It also can remedy the large gap of graphene between the low permeability and high complex permittivity. The presence of ACNTs increases the absorption bandwidth of the composite. Therefore, ACNT/RGO/BF composite has a good absorbing performance.

## 2. Experimentals

### 2.1 Synthesis and oxidation of ACNTs

The detailed method synthesis of ACNTs was reported in our previous article,[19,20] which performed by floating catalyst CVD in a quartz tube reactor (length 100 cm and diameter 60 mm). The reaction temperature was set at 770 °C, and argon gas with the flow speed of 200 sccm was used as the carrier gas. The xylene (analytical pure grade), ferrocene (analytical pure grade) and triethylsilane (analytical pure grade) solution (the mole ratio of C : Fe : Si is 300 : 10 : 1) was used as carbon source and catalyst precursor, which was injected into the reactor by a syringe pump at the speed of 0.3 ml min$^{-1}$. Then the obtained samples were added into the mixture of concentrated sulphuric acid and nitric acid (volume ratio = 3 : 1), finally treated with ultrasonic vibration for 8 h.

### 2.2 Preparation of GO

GO was prepared by a modified Hummers method. Briefly, first, the low temperature reaction stage, 1 g natural flake graphite (NFG) and $Na_2SO_3$ (analytical pure grade) mixed with 50 ml concentrated sulphuric acid were stirred by magnetic stirring apparatus in ice water bath. Then 6 g $KMnO_4$ (analytical pure grade) was slowly put into the solution in order to reduce the heat influence caused by the redox reaction. The reaction was maintained at this temperature for 1 h and the color of the solution was dark green in this step. Then followed by the middle temperature reaction stage, the beaker with the reactant was transferred to the water bath at 35 °C, stirring for 1 h. Finally, the high temperature reaction stage, the temperature of the water bath increased to 95 °C and meanwhile 80 ml distilled water was added to the solution slowly. The reaction time was 30 min in this stage. After the reaction, 200 ml distilled water was poured into the solution and added 6 ml $H_2O_2$ through drop by drop. Some bubbles appeared in the solution and the color changed into luminous yellow. The resulting sample was washed until neutral by centrifugal machine and then dried at 40 °C. The BF was synthesized by self-propagating combustion using citric acid complexed $Fe(NO_3)_3$ and $Ba(NO_3)_3$ as precursor and the mass ratio of $Fe(NO_3)_3$, $Ba(NO_3)_3$ and citric acid is 10 : 1 : 13. The ingredients were firstly dissolved into distilled water and then ammonium hydroxide was added to adjust pH = 7. The obtained colloidal sol was dried at 120 °C. The dried gel was heated at 400 °C for giving rise to the self-propagating combustion process. After the combustion reaction, the powders were collected and cleaned for further application.

### 2.3 Synthesis of interlinked ACNT/RGO/BF composites

The interlinked ACNT/RGO/BF composites were directly fabricated by self-propagating combustion method using the oxidized ACNTs, GO and citric acid mixed with $Fe(NO_3)_3$ (analytical pure grade) and $Ba(NO_3)_3$ (analytical pure grade) as precursor. The mass ratio of $Fe(NO_3)_3$, $Ba(NO_3)_3$ and citric acid is 10 : 1 : (6–15). The mass fraction of ACNTs or GO are various from 10 to 40 wt%. The ingredients were firstly dissolved into distilled water and then ammonium hydroxide was added to adjust pH = 7. The obtained colloidal sol was continuously heated and stirred at 350 °C to evaporate water and give rise to the self-propagating combustion process. After the combustion reaction, the interlinked ACNT/RGO/BF composites were synthesized. The GO was *in situ* reduced through the intense heat release during the reaction. The sample powders were collected and cleaned for further test and application.

### 2.4 Characterizations

Transmission electron microscope (TEM, Tecnai G2 F30, FEI), field emission scanning electron microscope (FE-SEM, JSM-6700F, JEOL), X-ray diffraction patterns with $CuK_\alpha$ radiation (XRD, X'Pert PRO MPD, PANalystal, $\lambda = 0.154$ nm) and the Raman scattering spectrum (514 nm, LabRAM HR800, HORIBA JOBIN YVON) are used for qualitative analyses on the surface morphology, microstructure and component composition of all samples. The samples which were used for the characterization of electromagnetic wave absorbing properties were prepared by mixing 20 wt% ACNT/RGO/BF composites with 80 wt% molten paraffin, then made into a rectangular waveguide (22.86 mm in length, 10.16 mm in width and 2 mm in thickness). The complex permittivity ($\varepsilon'$, $\varepsilon''$) and permeability ($\mu'$, $\mu''$) components as the function of frequency of a sample are measured using MS4644A Vector-Network Analyzer (VNA, Anritsu: 10 MHz to 40 GHz).

## 3. Results and discussion

Fig. 1 shows the morphology and structure characterization of ACNT/RGO/BF composites. Fig. 1(a) shows the low-magnification SEM image of BF without the adding of ACNTs or GO. It shows the obvious BF agglomeration morphology. Fig. 1(b) shows the high-magnification SEM image of ACNT/RGO/BF. ACNTs and RGO were homogeneously dispersed to

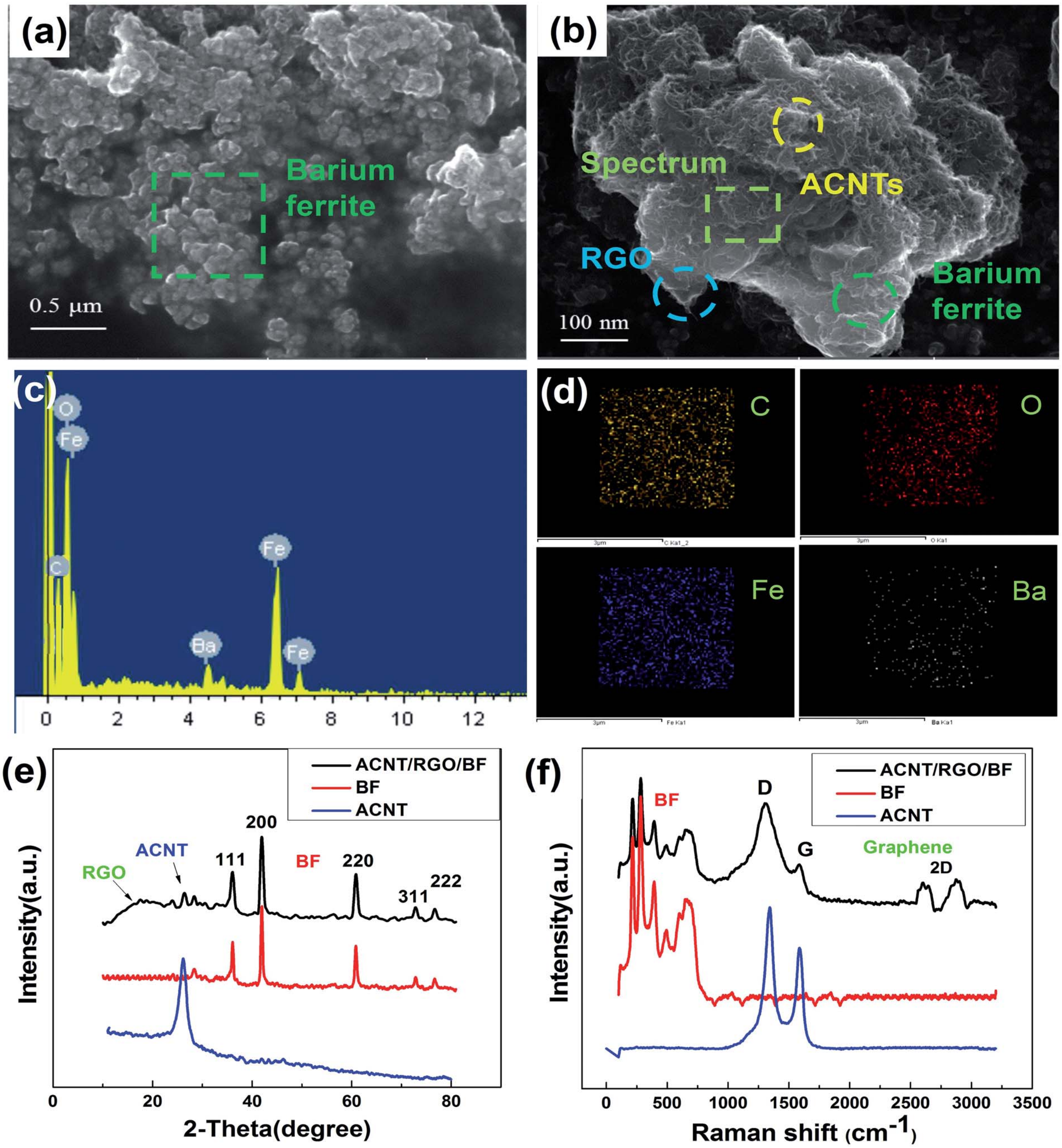

Fig. 1 Morphology and microstructure analysis of ACNT/RGO/BF composites (a) SEM image of BF; (b) SEM image of ACNT/RGO/BF; (c) EDS of ACNT/RGO/BF; (d) elemental mapping of ACNT/RGO/BF; (e) XRD spectrum; (f) Raman spectrum.

form interlinked conductive web structures inside the BF, which could increase the dielectric loss of the composite. Compared to Fig. 1(a), the BF morphology in Fig. 1(b) is not obvious, which might be due to the adding of ACNTs and RGO. Fig. 1(c and d) is the EDS analysis and elemental mapping [from Fig. 1(b) inset rectangular picture] of ACNT/RGO/BF composite. The adding content of Ba element is small so that the EDS peak is not very strong. The peak of Fe element is strong due to the large amounts of adding content. It also confirms the presence of C, O, Ba and Fe elements in the ACNT/RGO/BF composite. From the elemental mapping, the distribution of C, O, Ba and Fe are homogeneous indicating the ACNT/RGO and $BaFe_{12}O_{19}$ are mixed uniformly during the reaction process. Fig. 1(e) is XRD spectrum of ACNT/RGO/BF composite. The spectrum shows both the carbon peak causing by graphene/ACNTs (at around 20°) and the barium ferrite peaks. The BF has sharp peaks showing the high crystallinity. Fig. 1(f) is Raman spectrum of ACNT/RGO/BF composite. The spectrum has two obvious peaks centered at 1324.7 and 1593.2 cm$^{-1}$, namely D and G modes of CNTs. The D peak at 1324.7 cm$^{-1}$ stems from a symmetry-lowering effect due to the defects of nanotube and amorphous structures. The G peak at 1593.2 cm$^{-1}$ indicates the graphite crystallinity of this carbon material. The ratio of $I_D$ to $I_G$ is used to characterize the structure integrity of carbon materials. The ACNTs and RGO samples have a relative high ratio of $I_D/I_G = 1.387$ showing that there exist large amounts of defects in the structures. The ACNT/RGO/BF samples show the characteristic peak both barium ferrite (labeled in the image) and graphene/ACNTs. The presence of 2D peak proves the existence of graphene. The analysis results in Fig. 1(e and f) are in agreement with the results in Fig. 1(c and d).

Fig. 2 is the morphology and microstructure schematic diagram of ACNT/RGO/BF composite. Fig. 2(a) and (b) are TEM images of as-synthesized ACNTs before and after acidification treatment respectively. Before the acidification treatment, ACNTs intertwined randomly with a large number of catalyst particles and amorphous carbon nanoparticles are filled between the intertwined CNTs. After the acidification treatment, the catalyst and amorphous carbon particles are mostly removed. The purity of ACNTs is obviously improved. The agglomeration tendency of ACNTs decreases. ACNTs after the acidification treatment would have functional groups on the tube-wall of CNTs, which reduces the van der Waals' force between the ACNTs so as to increase the dispersitivity inside the barium ferrite. The grafted functional groups would also enhance the activity of CNTs connecting with the barium ferrite. Fig. 2(c) is the low-resolution TEM image of GO. The fluffy and transparent GO like tulle should has large specific surface. The graphene exhibits multiple layers and many folds. The edges partially curl with each other. Fig. 2(d) is high-resolution TEM image of GO. The atoms are randomly arranged. The diffraction ring of selected area electron diffraction (SAED) also shows the weak crystallinity. Fig. 2(e) is the TEM image of ACNT/RGO/BF composite. The schematic plot in Fig. 2(f) shows the interlinked structure of ACNTs and RGO inside barium ferrite. The formation of the intertwined networks increases the structure stability and the electrical conductivity for the electromagnetic wave absorbing properties.

The complex permittivity ($\varepsilon'$, $\varepsilon''$) and permeability ($\mu'$, $\mu''$) curves of ACNT/RGO/BF, RGO/BF and ACNT/BF composites *vs.* frequency are shown in Fig. 3(a–d). The permittivity and permeability are used for characterization of dielectric constant and magnetic loss properties of the electromagnetic wave absorbing materials. In Fig. 3(a and b), the dielectric constant ($\varepsilon'$) decreases slightly with frequency increasing. According to Koops theory based on the Maxwelle Wagner model for the inhomogeneous double layer dielectric structures, the well conductive grains in ferrous crystal are separated by the boundaries of poorly conductive grain. Here, in the formation of grain boundaries, the interaction between $BaFe_{12}O_{19}$ and CNTs or graphene plays an important role. At low frequencies, the grain boundaries are more effective than the conductive grains. Due to the high resistance of the grain boundaries, the hopping electrons will stack and produce polarization at these areas. The electronic conduction is high at low frequencies due to the polarization. However, the electron exchange between $Fe^{3+}$ and $Fe^{2+}$ ions cannot follow the fast alternating field, which decreases the probability of electrons reaching the grain boundaries and the interfacial polarization. In Fig. 3(a), the dielectric constant ($\varepsilon'$) of ACNT/RGO/BF and ACNT/BF is lower than that of RGO/BF composite, which might be due to the amorphous structure of ACNTs reduces the electrical conductivity of the composite. GO after the *in situ* high temperature reduction may have excellent conductivity. In Fig. 3(b), ACNT/RGO/BF composite has the highest dielectric loss ($\varepsilon''$). The ACNT/RGO network and BF structure have good dielectric polarization and relaxation effects. When the conductive phase is distributed in the insulating matrix to form composite materials, the free charges gathered in the interfaces between insulation and conductor due to the difference of two phase conductive performance. The interlinked net structures of ACNT/RGO may increase the probability of CNTs overlapping and twining each other so that the formed conductive networks inside $BaFe_{12}O_{19}$ could improve the dielectric polarization properties. Besides, the interlinked ACNT/RGO structures may also benefit the dielectric polarization properties and the large length-diameter ratio of CNTs is also beneficial to the conductivity and dielectric loss. In Fig. 3(c and d), it is worth noting that the minimum and maximum values are observed for $\mu'$ and $\mu''$, respectively, those obvious peaks for $\mu'$ and $\mu''$ can be ascribed to a resonance phenomenon, as shown in Fig. 3(f). The tendency of the lines in Fig. 3(c and d) is similar, because carbon nanomaterials have poor magnetic loss and all the several lines reveal the properties of $BaFe_{12}O_{19}$. The differences of real permeability among RGO/BF, ACNT/BF and ACNT/RGO/BF in 2–5 GHz might be due to the different content of ACNTs in these three composites. There might be the residual catalysts inside the ACNTs, which can cause the magnetic loss and influence the real permeability. The dielectric loss tangent is the main parameter to decide the electromagnetic performance of the composites. Here, the dielectric loss of ACNT/RGO/BF is the largest which is consistent with reflection loss result in Fig. 4.

$$R\ (\mathrm{dB}) = 20\log_{10}\left|\frac{Z_{\mathrm{in}}-1}{Z_{\mathrm{in}}+1}\right| \tag{1}$$

$$Z_{\mathrm{in}} = \left(\frac{\mu_{\mathrm{r}}}{\varepsilon_{\mathrm{r}}}\right)^{\frac{1}{2}}\tanh\left[\mathrm{j}\left(\frac{2\pi fd}{c}\right)(\mu_{\mathrm{r}}\varepsilon_{\mathrm{r}})^{\frac{1}{2}}\right] \tag{2}$$

The surface reflectivity of an absorber was presented by a function including six parameters of $\varepsilon'$, $\varepsilon''$, $\mu'$, $\mu''$, $f$ and $d$. Thus, if the six parameters are known, the absorbing properties of the material can be calculated. The values of reflection loss were calculated by using eqn (1) and (2) using the measured values of $\varepsilon'$, $\varepsilon''$, $\mu'$, $\mu''$, $f$ and $d$ (see Fig. 3). In the frequency range of 2–18 GHz, the reflection loss peak of ACNT/RGO/BF composite is −19.03 dB at 11.04 GHz in the frequency range of 2–18 GHz. The frequency bandwidth of the reflection loss below −10 dB is 3.8 GHz. For contrast, under the same matching thickness ($d_m = 2.0$ mm), the absorbing peaks of ACNT/BF and RGO/BF becomes more flat and wide. The reflection loss peak of ACNT/BF composite is about −14.99 dB at 9.04 GHz, the frequency bandwidth of the reflection loss below −10 dB is 1.52 GHz. The reflection loss peak of RGO/BF composite is about −8.14 dB at 13.6 GHz in the frequency

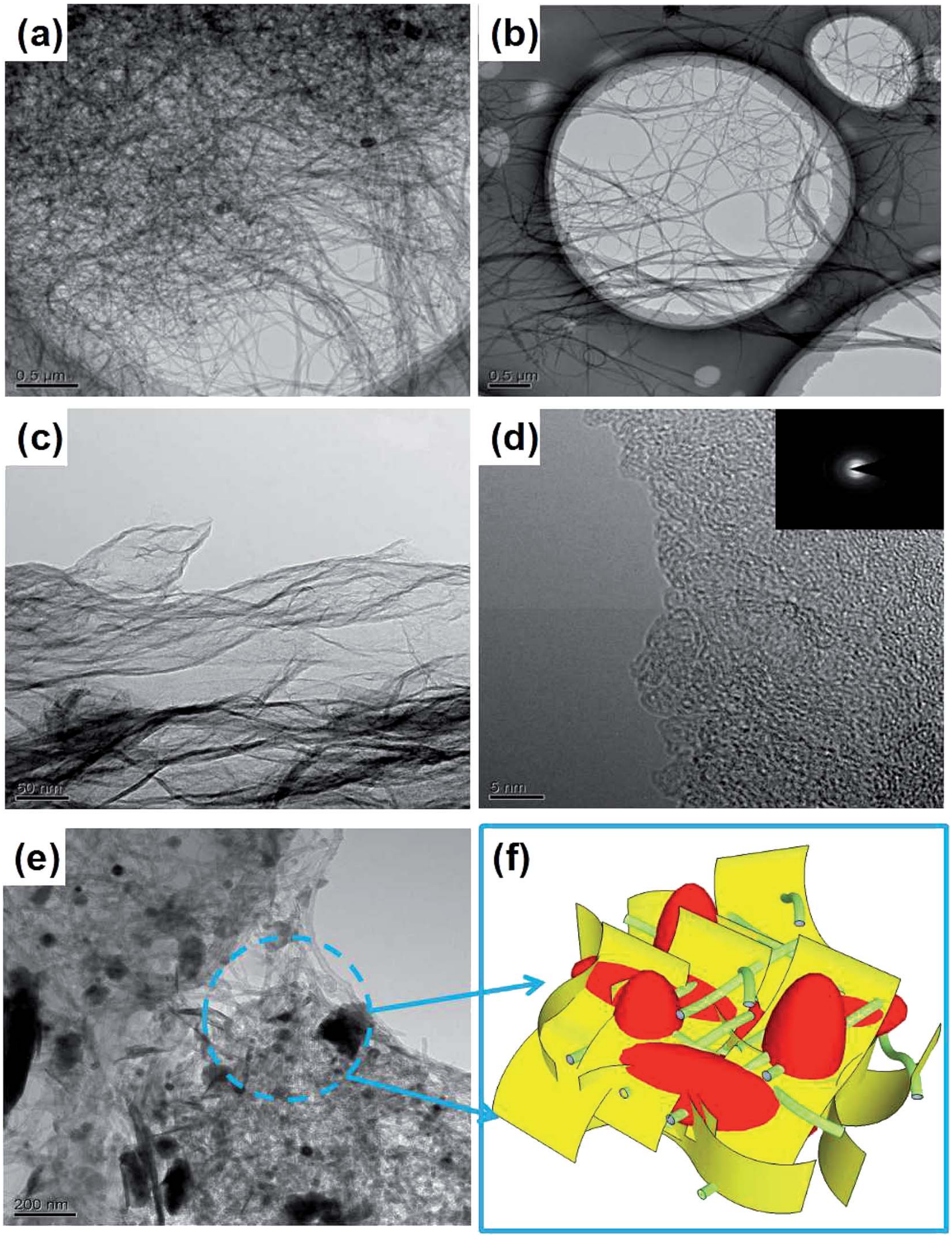

Fig. 2 Micromorphology and structure schematic diagram of ACNT/RGO/BF composite (a) TEM image of ACNTs before acidification; (b) TEM image of ACNTs after acidification; (c) and (d) TEM images of graphene; (e) TEM image of ACNT/RGO/BF composite; (f) the structure schematic diagram of interlinked ACNT/RGO/BF composite.

range of 2–18 GHz. It can also be proved through Fig. 3(e) that the dielectric loss tangent (tan $\delta_\varepsilon$) of ACNT/RGO/BF composite is much higher than that of RGO/BF as well as ACNT/BF. The schematic plot of the electromagnetic wave absorbing mechanism is shown in Fig. 4(c). The good electromagnetic wave absorbing properties of the interlinked ACNT/RGO network structures may be explained by the following several reasons. First, the conductive network structures with high density interlinked CNTs and RGO were formed inside barium ferrite, and it leads to more physical contacts between the conductive graphene sheets. So it also increases the resonance circuit density, which is consistent with the rising of electrical conductivity and dielectric loss tangent. The conductive networks would interact and attenuate the electromagnetic radiation in the absorbers effectively. The skin effect also affected the electromagnetic wave loss. Second, it exist the

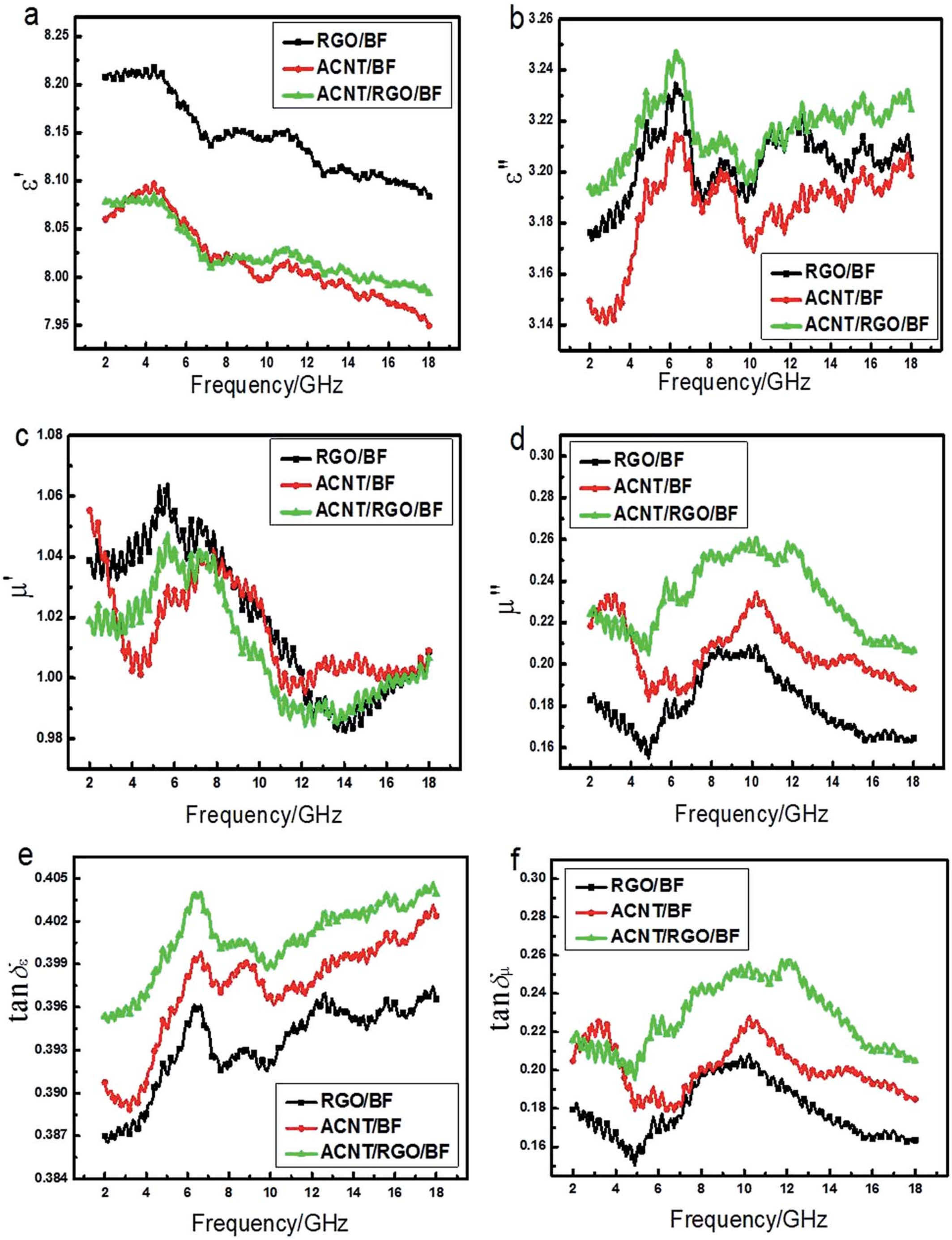

Fig. 3 Electromagnetic properties of ACNT/RGO/BF, RGO/BF and ACNT/BF composites *vs.* frequency. (a and b) The complex permittivity ($\varepsilon'$, $\varepsilon''$); (c and d) the complex permeability ($\mu'$, $\mu''$); (e) is the dielectric loss tangent (tan $\delta_\varepsilon$); (f) is the magnetic loss tangent (tan $\delta_\mu$).

polarization relaxation of defects or π-electron and the interfacial polarization between graphene and barium ferrite. ACNT/RGO structures with dense interlinked ACNTs can consume the incident waves through multiple reflections and scatterings.[21,22] The dihedral angles could be easily formed within carbon cluster stacks of ACNT tube walls, which cause multiple reflections of electromagnetic wave, prolonging the propagation path of electromagnetic waves in the absorbers. The multiple reflections of electromagnetic wave lead to the large losses of electromagnetic energy. Furthermore, the intertwined structures are consisting of interlinked ACNTs and graphene sheets spontaneously and intensely response to the broadband incident wave. It presents as tremendous resistance–inductance–capacitance coupled circuits. The interaction of electromagnetic waves with dielectric materials intensified the molecular motions such as ionic conduction, dipolar polarization

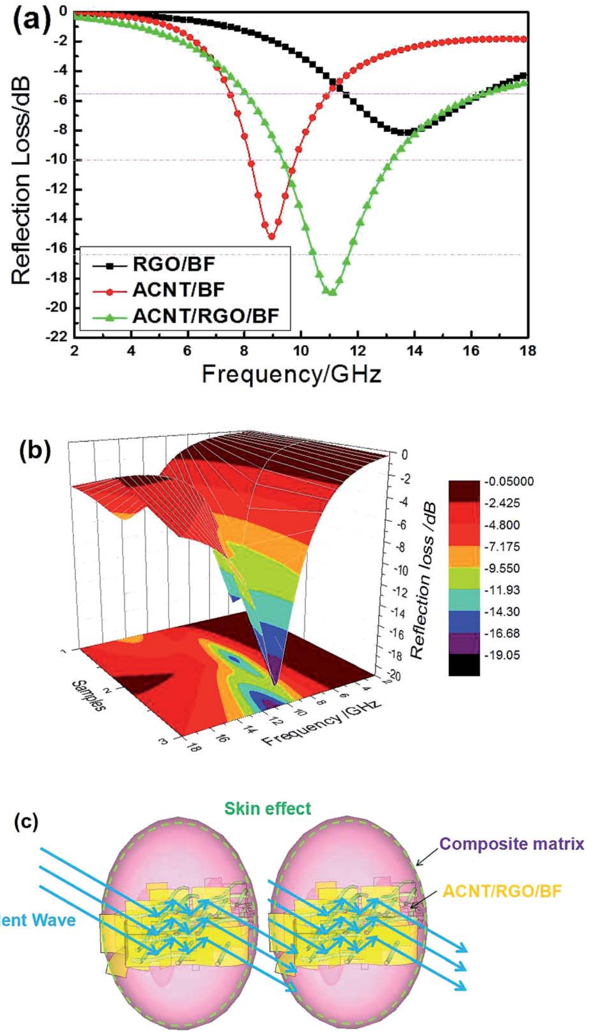

Fig. 4 Electromagnetic wave absorbing properties of ACNT/RGO/BF, RGO/BF and ACNT/BF composites (a) two-dimension; (b) three-dimension; (c) wave absorbing mechanism of ACNT/r-GO/BF composite.

relaxation, *etc.*, leading to energy dissipation in the form of heat through molecular friction and dielectric loss and the highly conductive networks would also consume the electromagnetic wave as resistance heat.

## 4. Conclusions

The as-synthesized ACNT/RGO/BF composites which have 3D network structures were directly prepared by self-propagation combustion process and used as absorber in the electromagnetic wave absorbing field. The reflection loss peak of ACNT/RGO/BF composite is −19.03 dB at 11.04 GHz in the frequency range of 2–18 GHz. The frequency bandwidth of the reflection loss below −10 dB is 3.8 GHz. The interlinked ACNT-RGO structures with dense intertwined graphene and ACNTs with quantities of dihedral angles could consume the incident waves through multiple reflection and scattering inside the web structures. The high conductivity of the interlinked ACNT/RGO networks would lead to energy dissipation in the form of heat through molecular friction and dielectric loss.

## Acknowledgements

This work was supported by the Natural Science Foundation of China (51572221, 51672221), China Aeronautical Science Fund (2014ZF53074), and the Key Science and Technology Program of Shaanxi Province, China (2013K09-03).

## References

1 T. B. Ghzaiel, W. Dhaoui, F. Schoenstein, P. Talbot and F. Mazaleyrat, Substitution effect of Me = Al, Bi, Cr and Mn to the microwave properties of polyaniline/$BaMeFe_{11}O_{19}$ for absorbing electromagnetic waves, *J. Alloys Compd.*, 2017, **1**, 774–786.
2 K. H. Tan, R. Ahmad and M. R. Johan, Electromagnetic and microwave absorbing properties of amorphous carbon nanotube-cadmium selenide quantum dot hybrids, *Mater. Chem. Phys.*, 2013, **139**, 66–72.
3 X. Sun, J. P. He, G. X. Li, J. Tang, T. Wang, Y. X. Guo and H. R. Xue, Laminated magnetic graphene enhanced electromagnetic wave absorption properties, *J. Mater. Chem. C*, 2013, **1**, 765–777.
4 C. Wang and X. J. Han, The electromagnetic property of chemically reduced graphene oxide and its application as microwave absorbing material, *Appl. Phys. Lett.*, 2011, **2**, 072906.
5 F. Hastings, J. Schneider and S. Broschat, Application of the perfectly matched layer (PML) absorbing boundary condition to elastic wave propagation, *J. Acoust. Soc. Am.*, 1996, **11**, 3061–3069.
6 X. Ding, Y. Huang, S. Li, N. Zhang and J. Wang, $FeNi_3$ nanoalloy decorated on 3D architecture composite of reduced graphene oxide/molybdenum disulfide giving excellent electromagnetic wave absorption properties, *J. Alloys Compd.*, 2016, **12**, 208–217.
7 H. Wang, H. H. Gao, M. X. Chen, X. Y. Xu, X. F. Wang, C. Pan and J. P. Gao, Microwave-assisted synthesis of reduced graphene oxide/titania nanocomposites as an adsorbent for methylene blue adsorption, *Appl. Surf. Sci.*, 2015, **360**, 840–848.
8 W. L. Song, X. T. Guan, L. Z. Fan, Y. B. Zhao, W. Q. Cao, C. Y. Wang and M. S. Cao, Strong and thermostable polymeric graphene/silica textile for lightweight practical microwave absorption composites, *Carbon*, 2016, **100**, 109–117.
9 X. Huang, X. Yan, L. Xia, P. Wang, Q. Wang, X. Zhang, B. Zhong, H. Zhao and G. Wen, A three-dimensional graphene/$Fe_3O_4$/carbon microtube of sandwich-type architecture with improved wave absorbing performance, *Scr. Mater.*, 2016, **120**, 107–111.
10 C. H. Wang, Y. J. Ding, Y. Yuan, X. D. He, S. T. Wu, S. Hu, M. C. Zou, W. Q. Zhao, L. S. Yang, A. Y. Cao and Y. B. Li, Graphene aerogel composites derived from recycled

cigarette filters for electromagnetic wave absorption, *J. Mater. Chem.*, 2015, **3**, 11893–11901.

11 L. Chen, R. Du, J. H. Zhu, Y. Y. Mao, C. Xue, N. Zhang, Y. L. Hou, J. Zhang and T. Yi, Three-dimensional nitrogen-doped graphene nanoribbons aerogel as a highly efficient catalyst for the oxygen reduction reaction, *Small*, 2015, **3**, 1423–1429.

12 R. S. Meena, S. Bhattachrya and R. Chatterjee, Complex permittivity, permeability and wide band microwave absorbing property of La substituted U-type hexaferrite, *J. Magn. Magn. Mater.*, 2010, **322**, 1923–1928.

13 T. C. Zou, H. P. Li, N. Q. Zhao and C. S. Shi, Electromagnetic and microwave absorbing properties of multiwalled carbon nanotubes filled with Ni nanowire, *J. Alloys Compd.*, 2010, **496**, 22–24.

14 A. Ghasemi, S. E. Shirsath, X. Liu and A. Morisako, A comparison between magnetic and reflection loss characteristics of substituted strontium ferrite and nanocomposites of ferrite/carbon nanotubes, *J. Appl. Phys.*, 2012, **111**, 07B543.

15 T. K. Zhao, C. L. Hou, H. Y. Zhang, R. X. Zhu, S. F. She, J. G. Wang, T. H. Li, Z. F. Liu and B. Q. Wei, Electromagnetic wave absorbing properties of amorphous carbon nanotubes, *Sci. Rep.*, 2014, **4**, 5619.

16 A. Ghasemi, X. Liu and A. Morisako, Magnetic and microwave absorption properties of $BaFe_{12-x}(Mn_{0.5}Cu_{0.5}Zr)_{x/2}O_{19}$ synthesized by sol–gel processing, *J. Magn. Magn. Mater.*, 2007, **316**, 105–108.

17 G. Mu, N. Chen, X. Pan, H. Shen and M. Gu, Preparation and microwave absorption properties of barium ferrite nanorods, *Mater. Lett.*, 2008, **62**, 840–842.

18 J. Li, H. W. Zhang, Q. Li, Y. X. Li and G. L. Yu, Influence of La–Co substitution on the structure and magnetic properties of low-temperature sintered M-type barium ferrites, *J. Rare Earths*, 2013, **10**, 983–987.

19 T. K. Zhao, X. L. Ji, H. Z. Liu, P. Y. Yao, W. J. Liu, C. Y. Xiong, T. X. Li and C. Wang, Growth of well-aligned carbon nanotubes with different shapes, *Appl. Surf. Sci.*, 2015, **357**, 2136–2140.

20 T. K. Zhao, X. L. Ji, W. B. Jin, S. S. Guo, H. Y. Zhao, W. H. Yang, X. Q. Wang, C. Y. Xiong, A. L. Dang, H. Li, T. H. Li, S. M. Shang and Z. F. Zhou, Electromagnetic wave absorbing properties of aligned amorphous carbon nanotube/$BaFe_{12}O_{19}$ nanorod composite, *J. Alloys Compd.*, 2017, **703**, 424–430.

21 V. K. Singh, A. Shukla, M. K. Patra, L. Saini, R. K. Jani, S. R. Vadera and N. Kumar, Microwave absorbing properties of a thermally reduced graphene oxide/nitrile butadiene rubber composite, *Carbon*, 2012, **50**, 2202–2208.

22 L. Wang, H. L. Xing, S. T. Gao, X. L. Ji and Z. Y. Shen, Porous flower-like NiO@graphene composites with superior microwave absorption properties, *J. Mater. Chem. C*, 2017, **1**, 1–10.